The assembly of 'normal' galaxies at $z \sim 7$ probed by ALMA

R. Maiolino,[1,2]* S. Carniani,[1,2,3] A. Fontana,[4] L. Vallini,[5,6] L. Pentericci,[4] A. Ferrara,[5]
E. Vanzella,[7] A. Grazian,[4] S. Gallerani,[5] M. Castellano,[4] S. Cristiani,[8] G. Brammer,[9]
P. Santini,[4] J. Wagg[10] and R. Williams[1,2]

[1]*Cavendish Laboratory, University of Cambridge, 19 J. J. Thomson Ave, Cambridge CB3 0HE, UK*
[2]*Kavli Institute for Cosmology, University of Cambridge, Madingley Road, Cambridge CB3 0HA, UK*
[3]*Dipartimento di Fisica e Astronomia, UniversitàÅ di Firenze, Via G. Sansone 1, I-50019 Sesto Fiorentino (Firenze), Italy*
[4]*INAF – Osservatorio Astronomico di Roma, via Frascati 33, I-00040 Monteporzio, Italy*
[5]*Scuola Normale Superiore, Piazza dei Cavalieri 7, I-56126 Pisa, Italy*
[6]*Dipartimento di Fisica e Astronomia, UniversitÃă di Bologna, viale Berti Pichat 6/2, I-40127 Bologna, Italy*
[7]*INAF – Bologna Astronomical Observatory, via Ranzani 1, I-40127 Bologna, Italy*
[8]*INAF – Trieste Astronomical Observatory, via Tiepolo 11, I-34143 Trieste, Italy*
[9]*Space Telescope Science Institute, 3700 San Martin Drive, Baltimore, MD 21218, USA*
[10]*Square Kilometre Array Organization, Jodrell Bank Observatory, Lower Withington, Macclesfield, Cheshire SK11 9DL, UK*

ABSTRACT

We report new deep observations obtained with the Atacama Large Millimetre Array (ALMA) aimed at investigating the [C II]158 μm line and continuum emission in three spectroscopically confirmed Lyman break galaxies at $6.8 < z \leq 7.1$, i.e. well within the re-ionization epoch. With star formation rates of SFR $\sim$ 5–15M$_\odot$ yr^{-1} these systems are much more representative of the high-z galaxy population than other systems targeted in the past by millimetre observations. For the galaxy with the deepest observation we detect [C II] emission at redshift $z = 7.107$, fully consistent with the Ly α redshift, but spatially offset by 0.7 arcsec (4 kpc) from the optical emission. At the location of the optical emission, tracing both the Ly α line and the far-UV continuum, no [C II] emission is detected in any of the three galaxies, with 3σ upper limits significantly lower than the [C II] emission observed in lower redshift galaxies. These results suggest that molecular clouds in the central parts of primordial galaxies are rapidly disrupted by stellar feedback. As a result, [C II] emission mostly arises from more external accreting/satellite clumps of neutral gas. These findings are in agreement with recent models of galaxy formation. Thermal far-infrared continuum is not detected in any of the three galaxies. However, the upper limits on the infrared-to-UV emission ratio do not exceed those derived in metal- and dust-poor galaxies.

Key words: galaxies: evolution – galaxies: formation – galaxies: high-redshift – galaxies: ISM – galaxies: star formation.

1 INTRODUCTION

Millimetre and submillimetre observations of distant galaxies are a powerful tool to trace the evolution of the gas and dust content (e.g. Daddi et al. 2010; Genzel et al. 2010; Bothwell et al. 2013; Carilli & Walter 2013; Tacconi et al. 2013; Santini et al. 2014), to investigate their dynamics (e.g. Carilli et al. 2013; Carniani et al. 2013; Wang et al. 2013; Willott, Omont & Bergeron 2013; De Breuck et al. 2014; Willott, Bergeron & Omont 2015a) to trace obscured star formation (e.g. Negrello et al. 2010; Gallerani et al. 2012; Hezaveh et al. 2013; Swinbank et al. 2014; Schaerer et al. 2015a), and even

to trace AGNs and their effect on to their host galaxy (Maiolino et al. 2012; Gallerani et al. 2014; Cicone et al. 2015).

Molecular (mostly CO) transitions are used to trace the content of molecular gas, while continuum emission is used to trace warm dust heated by ongoing star formation (and possibly by an AGN). At $z > 4$ millimetre and submillimetre observations are even more effective since the luminous [C II]158 μm far-infrared fine structure line is redshifted into the primary bands of atmospheric transmission, at frequencies $\nu < 350$ GHz (Maiolino et al. 2005, 2009; Walter et al. 2009; De Breuck et al. 2011). The [C II]158 μm line is one of the main coolants of the interstellar medium (ISM), both in local and high-z galaxies, generally excited by heating of UV photons in star-forming regions, primarily associated with their photodissociation regions (PDRs; Madden et al. 1997; Kaufman

Table 1. Sample and parameters of resulting from the observations.

Name	RA(J2000) (deg)	DEC(J200) (deg)	$z_{\text{Ly}\alpha}$	SFR[a] ($M_\odot$ yr^{-1})	ν_{obs}([C II])[b] (GHz)	Beam[c] [min (arcsec) ×maj (arcsec) (PA°)]	t_{on}(int.)[d] (h)	antennas	σ_{cont}^{e} (µJy)	σ_{line}^{f} (mJy)	L([C II])[g] (10^7 $L_\odot$)
BDF-3299	337.0511	−35.1665	7.109[h]	5.7	234.374	0.55 × 0.76 (85)	5.1	25–36	7.8	0.062	<2.0
BDF-512	336.9444	−35.1188	7.008[h]	6.0	237.330	0.72 × 0.50 (68)	1.4	29	17.4	0.171	<6.0
SDF-46975	200.9292	+27.3414	6.844[i]	15.4	242.290	0.96 × 0.82 (79)	2.0	40	19.2	0.173	<5.7

Notes. [a]This is the SFR inferred from the rest-frame UV continuum and is adapted to the new calibration given in Kennicutt & Evans (2012), who adopt a Kroupa IMF. [b]Expected redshifted frequency of [C II] [Local Standard of Rest Kinematic (LSRK)] from the Ly α redshift. [c]This column gives the synthesized beam (median value across SW1) minor and major axes (in arcsec) and position angle (in degrees, anticlockwise relative to the north). [d]On-source integration time (in hours). [e]rms on the continuum. [f]rms measured in the spectrum extracted from the central beam, avoiding regions of higher noise associated with atmospheric absorption (except for SDF-46975, see text), in spectral channels of 100 km s^{-1}. [g]The upper limits on the [C II] luminosities are at 3σ, and are calculated on a width of 100 km s^{-1}. [h]From Vanzella et al. (2011). [i]From Ono et al. (2012).

et al. 1999; Graciá-Carpio et al. 2011; Pineda, Langer & Goldsmith 2014), although contribution from diffuse atomic and partially ion-ized gas, as well as from shocked gas, has been inferred in some galaxies (Cormier et al. 2012; Appleton et al. 2013; Pineda et al. 2014; Velusamy & Langer 2014).

Until recently, at $z > 4$ [C II], CO and continuum emission had been detected only in extreme galaxies such as quasar hosts or sub-millimeter galaxies (SMGs), characterized by star formation rates (SFR) of the order of 1000 $M_\odot$ yr^{-1}, certainly not representative of the bulk of the galaxy population. In the last few years a few galax-ies at $z \sim 4$–6 with more modest SFR (20–300 $M_\odot$ yr^{-1}) have been detected in [C II] or in continuum (Wagg et al. 2012; Carilli et al. 2013; Carniani et al. 2013; Riechers et al. 2014; Williams et al. 2014). It should be noted that even these SFR are not yet really representative of the bulk of galaxies in the early Universe, which have SFR typically lower than 10 $M_\odot$ yr^{-1} (Salvaterra, Ferrara & Dayal 2011; Finkelstein et al. 2012; Dayal et al. 2014; Robertson et al. 2015). At $z \sim 7$, well within the re-ionization epoch, only one quasar host galaxy has been detected in [C II] and in continuum (at $z = 7.08$; Venemans et al. 2012). 'Normal' galaxies at $z \sim 7$, with SFR more representative of the galaxy population at these early epochs, have not yet been detected either in [C II] or in continuum (González-López et al. 2014; Ota et al. 2014; Schaerer et al. 2015b). We also note that $z \sim 7.7$ is the maximum redshift at which galaxies are spectroscopically confirmed (Oesch et al. 2015) and we recall that, even with the broad ALMA band, a spectroscopic redshift is needed to observe far-IR transitions redshifted into the millimetre band.

We have undertaken an ALMA programme targeting a sample of three spectroscopically confirmed galaxies at $6.8 < z < 7.1$ with the aim of detecting or constraining both the [C II] line and the continuum thermal emission.

For consistency with other papers on similar sources, we assume the following cosmological parameters: $H_0 = 70$ km s^{-1} Mpc^{-1}, $\Omega_\Lambda = 0.7$ and $\Omega_m = 0.3$.

2 SAMPLE SELECTION, OBSERVATIONS AND DATA ANALYSIS

The list of galaxies observed is given in Table 1. These targets were initially selected as Lyman Break Galaxies through their z–Y dropout (Castellano et al. 2010; Ono et al. 2012) and all of them have solid spectroscopic confirmations, through the detection of Ly α with clearly asymmetric profile due to absorption of the blue side by the intervening IGM (Vanzella et al. 2011; Ono et al. 2012).

The redshift given in Table 1 refers to the redshift inferred from the peak of the Ly α emission. This is probably significantly in

excess (even by a few 100 km s^{-1}) with respect to the real systemic redshift of the sources, because of IGM absorption of the blue side of Ly α, and possibly also because of the effect of outflows (e.g. Pettini et al. 2002). The quoted SFR are based on their UV emission, assuming no dust extinction (which however is likely to be very low given the very steep UV continuum; Vanzella et al. 2011). We have also corrected them, relative to the original papers, by adopting the new relation provided by Kennicutt & Evans (2012, who use a Kroupa initial mass function, IMF).

The ALMA observations were obtained between 2013 October and 2014 April, with a number of antennas ranging from 26 to 40, depending on the specific observation (by also taking into account the fact that a few noisy antennas were removed – flagged as 'bad'– from further reduction). An early observation of BDF3299 in 2013 May was not considered, because it was much noisier than the other data. The antennas were distributed in a semicompact configura-tion, with most of them within about 200 m from the array centre, but with one or two antennas located as far as 500–1000 m. The precipitable water vapour during the observations ranged between 0.9 and 1.8 mm, with an average of about 1.2 mm.

Observations were performed in Frequency Division Mode. Out of the four spectral windows, SPW1 was always centred on the expected frequency of the [C II] line, in the Upper Side Band. This spectral band was set to a spectral resolution of 2.5 km s^{-1}. SPW0 was located on the continuum next to SPW1 (on the higher fre-quency side), while SPW2 and SPW3 were located in the Lower Side Band to sample the continuum. The spectral resolution of the 'continuum' spectral bands was different depending on the specific observation.

The phases were centred at the nominal optical position of the source (but see discussion below about astrometric offset between optical and millimetre data for BDF3299).

The band pass calibrators for BDF3299 and BDF512 were J2056−4714 and J2258−2758, while for SDF46975 the bandpass calibrator was J1331+3030. The flux calibrator for BDF3299 and BDF521 was Neptune, while the flux calibrator for SDF46975 were Ceres and Pallas. The phase calibrators for BDF3299 and BDF521 were J2223−3137 and J2247−3657, while the phase calibrator for SDF46975 was J1058+0133.

We note that the observations of BDF3299 were obtained in two different runs, one in 2013 October/November and one in 2014 April. For the 2014 April observations, we moved the central fre-quency of SPW1 by about 100 km s^{-1} with respect to the observa-tion in 2013 October and also the phase centre was offset by about 0.6 arcsec. Therefore, before combining the data, the data obtained in 2014 April were phase-shifted to match the phase centre of the observations in 2013 October.

The ALMA data were reduced and analysed by using CASA version 4.2.1. Unfortunately this CASA version does not assign physically based weights to data taken at different epochs, with different integrations times, different atmospheric opacities and with different spectral resolutions. As a consequence, before combining the visibilities of two observations at two different epochs, we manually re-scaled their relative weights so that they matched the noise variance measured in the two cubes. For the same reason, the same process had to be applied when combining data from different spectral windows (e.g. to generate the continuum maps) taken with different spectral resolution, i.e. the weights of the different spectral windows (when taken with different resolutions) had to be adjusted manually.

The cubes were created with natural weighting and by shifting the channels to a common velocity reference (i.e. by setting mode='velocity' in the CASA *clean* command).

The resulting cubes images typically have a beam size of about 0.7 arcsec, yet the detailed beam shape and orientation for each observation is given in Table 1. No cleaning was performed in any cube, since there are no sources bright enough in the field of view. The only exception is the continuum image of BDF3299, in which a 400 μJy serendipitous source is detected and which has enabled us to perform the cleaning (with 500 iterations) of the continuum map.

The primary beam full width at half-maximum (FWHM) at this frequency is 22 arcsec.

The continuum maps were obtained by collapsing the four spectral windows (by taking care of the proper weighting between spectral windows with different channel widths, as discussed above).

The final sensitivity reached in each set of data is given in Table 1, both for the continuum and for spectral bins (as detailed in the following). In the deepest cube (the one on BDF3299) we reach a continuum sensitivity of 7.8 μJy by using the equivalent full spectral band of 7.8 GHz. The sensitivity to line detection depends on the specific frequency, since each band is affected by atmospheric absorption in some spectral regions. The sensitivity also depends on the spatial location, both because of the shape of the primary beam, which decreases the sensitivity at large radii from the phase centre, and because continuum serendipitous sources may generate sidelobes in their vicinity. In Table 1, we give the rms in spectral bins of 100 km s^{-1} obtained by extracting the spectrum on the central beam (phase centre) and taking the rms spectrally, in the spectral region close to the expected frequency of the [C II] line. The latter may require the selection of different spectral ranges depending of the source, because of the different location of the atmospheric absorption features in different spectra (relative to the expected [C II] frequency). In the cases of BDF3299 and BDF521 the expected location of the [C II] line is in an excellent atmospheric region. In these cases, we have measured the rms of the spectrum between −1000 and +300 km s^{-1}; outside this range the rms increases as a consequence of atmospheric absorption features. In the case of SDF46975, an atmospheric absorption feature is located just redward of the expected [C II] frequency from the Ly α redshift; since we do not know exactly the expected location of the [C II] from the real accurate redshift, we conservatively estimate the noise from the spectral range corresponding to the atmospheric absorption feature.

The absolute astrometric accuracy of the maps is given by the accuracy of the phase calibration and the accuracy of the absolute coordinates of the phase calibrator. The global absolute astrometric uncertainty is estimated to be about 0.15 arcsec. In the case of BDF3299, two observations were performed with two different phase calibrators: in the two observations the continuum

serendipitous sources have the same absolute position within less than 0.1 arcsec, confirming the accuracy of the absolute astrometric calibration of ALMA.

The absolute astrometric accuracy is only relevant for the comparison with the *Y*-band images. In the case of BDF3299 the ALMA data reveal two serendipitous continuum sources detected at high level of significance (Carniani et al. 2015), both of which have a clear counterpart in the *Y*-band image or in the *K*-band image (which is cross-matched with the *Y* band). However, both optical and near-IR counterparts are offset by about the same amount in the same direction relative to the ALMA continuum sources, and more specifically by ∼0.4 arcsec towards the NW (PA∼343°). Such a systemic offset is shown and discussed in Appendix A. Since these offsets are the same for both continuum sources we believe they are associated with an offset of the astrometry of the near-IR images relative to the ALMA images (we shall mention that the absolute astrometry of the *Y*-band and *K*-band images is linked to the United States Naval Observatory B (USNO-B) catalogue, which has an average absolute astrometric accuracy of 0.25 arcsec at the epoch J2000, but variable across the sky with a dispersion about 0.12 arcsec). Therefore, when comparing with the *Y*-band image, we will apply to the *Y*-band image an offset of 0.4 arcsec to the SE (PA = 163°).

3 [C II] EMISSION AT THE LOCATION OF THE OPTICAL SOURCES

The [C II] line is not detected (at a confidence higher than 3σ) in any of the three sources at the location of their *Y*-band emission (i.e. within a radius 0.5 arcsec from the latter). We recall that in these sources the *Y*-band emission is partly contributed by UV stellar continuum emission and partly by Ly α emission (at least for BDF521 and BDF3299, Ly α and UV continuum contribute to 1/3 and 2/3, respectively, of the observed *Y*-band flux; Vanzella et al. 2011).

The spectra extracted from the central beam are shown in Fig. 1, along with the spectral distribution of the noise in the lower panels.

To estimate the upper limit on the line flux we assume a line width of 100 km s^{-1} (we will see in the next section that this is the velocity width of the [C II] clump detected next to BDF3299, moreover this width is consistent with other lower redshift galaxies with low SFR, e.g. Williams et al. 2014; Capak et al. 2015). Note that other authors provide upper limits by assuming a line width of 40 km s^{-1} (González-López et al. 2014; Ota et al. 2014); since these data will be used in our analysis, we have re-scaled their upper limits to a line width of 100 km s^{-1} for consistency (this is simply done by assuming that the noise on the line flux scales as the square root of the line width). The 3σ upper limits on the [C II] luminosity are given in Table 1.

Since [C II] is primarily excited as a consequence of heating by soft-UV radiation (mostly in PDRs associated with star-forming regions, but also in H II regions or in the diffuse medium), many authors have identified a correlation between SFR and [C II] luminosity (e.g Sargsyan et al. 2012; De Looze et al. 2014).

If the far-IR luminosity is used to measure the SFR, then the correlations seems to break down at high far-IR luminosities [in the range of ultra-luminous infrared galaxies (ULIRGs)] and it is not yet clear whether this is associated with an additional contribution to the far-IR from powerful AGNs, hence resulting in an inappropriate measurement of the SFR from the far-IR emission (Malhotra et al. 2001; Sargsyan et al. 2012), or associated with different physical conditions in ULIRGs, which may suppress the emission of [C II] (Kaufman et al. 1999; Graciá-Carpio et al. 2011). However, our
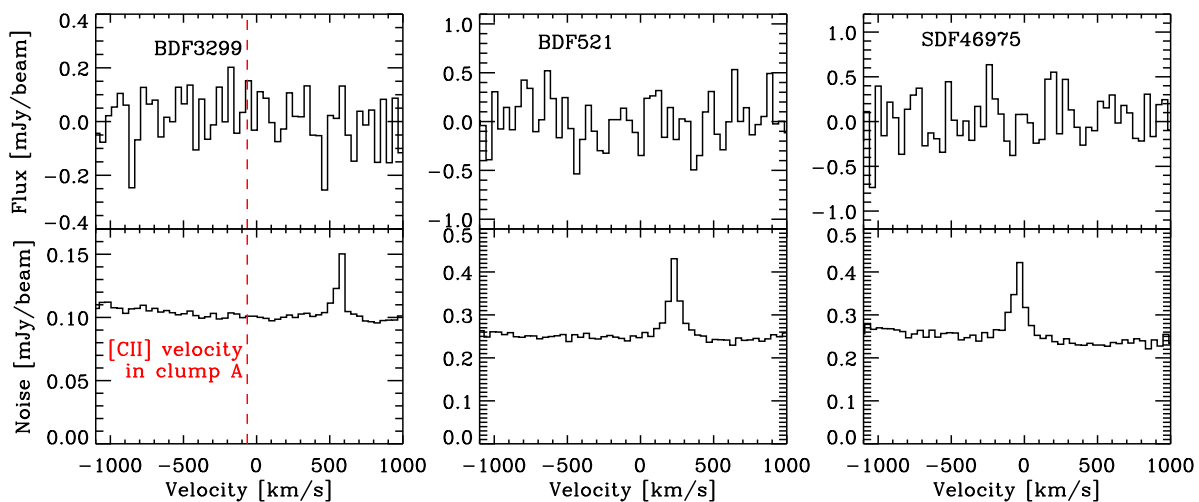
Figure 1. Top: spectra of the three sources in our sample, centred at the location of the optical counterpart, extracted from the central beam. The velocity reference is set to the redshift defined by the Ly α peak. Bottom: noise in the same velocity range measured across each plane associated with each spectral bin. The regions where the noise is higher are associated with spectral regions of telluric absorption. The spectral binning of these spectra is $40\,\mathrm{km\,s^{-1}}$. The vertical red dashed line in the leftmost panel indicates the velocity of the [C II] line detected next to BDF3299 in clump 'A', illustrating that the line is located in a region of low noise.
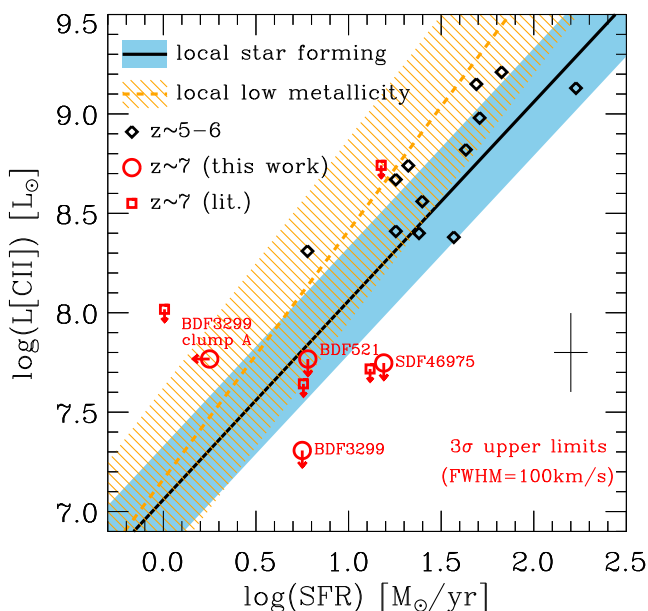

Figure 2. [C II]158 μm luminosity versus SFR. The blue line shows the relation found by De Looze et al. (2014) for local star-forming galaxies and starbursts (non-including ULIRGs), while the shaded region shows the 1σ dispersion. The orange dashed line and hatched region show the relation and dispersion found by De Looze et al. (2014) for local low metallicity dwarfs and irregulars. The black diamonds are galaxies at $z \sim 5$–6 from Capak et al. (2015) and Willott et al. (2015b) and their average error bar is shown in the bottom-right of the diagram. The red symbols are the [C II] data for galaxies at $z \sim 7$ (specifically at $6.8 < z < 11$): circles are our new observations and squares are data from the literature (González-López et al. 2014; Ota et al. 2014; Schaerer et al. 2015b).

sources are certainly not in the ULIRG luminosity range, so we will not consider the latter issue any further.

Fig. 2 shows the L([C II]) versus SFR relation for various classes of galaxies presented in De Looze et al. (2014). The blue line

indicates the relation for local normal star-forming and starburst (non-ULIRG) galaxies, with the shaded blue region giving the $\pm 1\sigma$ dispersion. The orange dashed line and hatched region show the relation and dispersion of local low metallicity galaxies (in the range $\frac{1}{40} < Z/Z_\odot < 1$). For many of the low metallicity galaxies in the sample of De Looze et al. (2014) the L([C II])/SFR ratio tends to be even higher than in normal galaxies (this is mostly a consequence of [C II] being a coolant of the ISM), however at very low metallicities ($Z < 0.1\ Z_\odot$) the L([C II])/SFR start to decrease and becomes lower than in normal galaxies. at high-z, despite Ly α being relatively broad (Williams et al. 2014).

Galaxies at $5 < z < 6.1$, from Capak et al. (2015) and Willott et al. (2015b), are shown with black diamonds and tend to follow the same [C II]/SFR relation as local galaxies. These galaxies, with SFR typically of a few/several times 10 $M_\odot$ yr^{-1} are not yet representative of the bulk of the population at these redshifts (Salvaterra et al. 2011; Finkelstein et al. 2012; Dayal et al. 2014; Robertson et al. 2015).

The 3σ upper limits for 'normal' galaxies at $z \sim 7$ (those with SFR < 100 $M_\odot$yr^{-1}, i.e. not including the extreme quasar at $z = 7.08$) are indicated with red symbols in Fig. 2. Circles indicate our new observations, while squares are for additional galaxies at $6.8 < z < 11$ from previously published studies (González-López et al. 2014; Ota et al. 2014; Schaerer et al. 2015b). At least three galaxies at $z \sim 7$ for which a meaningful constraint on L([C II]) has been obtained (including our ALMA deepest observation, BDF3299) have, at a given SFR, a 3σ upper limit on their [C II] luminosity significantly lower than observed in most galaxies at lower redshifts, even by including the low metallicity ones.

However, we note that the lowest metallicity local galaxies in the De Looze et al. (2014) sample ($Z \sim 0.1$–0.02 $Z_\odot$) have [C II]/SFR values comparable with the 3σ upper limit on BDF3299 (although they have much lower SFR). Therefore, in principle, such a [C II] line deficit in $z \sim 7$ normal galaxies could be ascribed to low metallicity. Low metallicity of high-z galaxies has been a possible interpretation for the lack of [C II] detection in some star-forming galaxies at $z \sim 6.5$ (Ouchi et al. 2013; Vallini et al. 2013). Yet, one

should bear in mind that the intensity of the [C II] line, as many other coolants of the ISM, does not scale linearly with metallicity (see e.g. Röllig et al. 2006; Madden et al. 2011; Nagao et al. 2011; Cormier et al. 2012). Most importantly, we will show in the next section that [C II] emission is actually detected in a gas clump next to BDF3299. Therefore, while metallicity may play a role, it is probably not the only origin of the [C II] deficiency in the core of these primeval galaxies, as discussed in the following.

4 [C II] EMISSION NEXT TO BDF3299 AT $z = 7.1$

4.1 Line detection

In the ALMA cube of BDF3299, which is the deepest of our observations, we have detected a line consistent with [C II] at the redshift, $z = 7.1$, inferred from the Ly α of the galaxy (especially once IGM absorption of Ly α is taken into account), but offset by 0.7 arcsec (i.e. 4 kpc) relative to the location of the primary galaxy in the Y-band image (which traces UV+Ly α emission).

The map of the line emission is shown in Fig. 3, extracted with a spectral width of $100 \, \text{km s}^{-1}$ and centred at $-64 \, \text{km s}^{-1}$, relative to the velocity scale set by the redshift inferred from Ly α. The white cross indicates the centroid of the Y-band image of BDF3299.

The [C II] emitting clump is marked with an 'A' and is located at RA(J2000)=22:28:12.325, Dec.(J2000)=−35:10:00.64. Its emission peak is detected at 4.5σ. However, the source is marginally resolved (along a Position Angle of $-33°.5$) hence the significance cannot be inferred simply by the peak surface density in units of flux per beam. In this case, as for extended sources, to properly assess the significance of the detection, we have to extract the spectrum of the source. We have first fitted a two-dimensional Gaussian to the [C II] emission, and then extracted the spectrum from an aperture corresponding to the section of the ellipsoid at half-maximum of its peak (i.e. an ellipses which has minor and major axes of 0.55 arcsec and 1.03 arcsec, respectively). Since the extraction aperture has a size close to the beam, we have applied a flux aperture correction (inferred from the flux extracted with the same aperture from the continuum serendipitae), which results to be a factor of 2.5. The resulting spectrum is shown in Fig. 4, rebinned to $40 \, \text{km s}^{-1}$, together with the optical spectrum of Ly α. The line has a peak at a velocity of $-71 \, \text{km s}^{-1}$ relative to the Ly α peak.[1] As already mentioned, such a velocity offset is expected. Indeed the Ly α is redshifted relative to the systemic velocity as a consequence of IGM absorption (as clearly shown by its strongly asymmetric profile), and possibly also due to the effect of outflows (e.g. Pettini et al. 2002), hence the real redshift of BDF3299 is certainly slightly lower than inferred from Ly α. Therefore, the blueshift by $-71 \, \text{km s}^{-1}$ is fully consistent with the rest frame of the galaxy. We have measured the significance of the line by measuring the noise in the spectrum between $-1000 \, \text{km s}^{-1}$ and $+300 \, \text{km s}^{-1}$; this is a region with uniform, low noise, while outside this spectral range atmospheric absorption makes the noise higher (see Fig. 1). To avoid any potential baseline residual instability, we have also subtracted a continuum fitted on the same spectral window (which however is consistent with zero within the noise). By integrating the line under the shaded region in Fig. 4 ($-200 < \text{V} < 0 \, \text{km s}^{-1}$), we obtain a significance of the detection
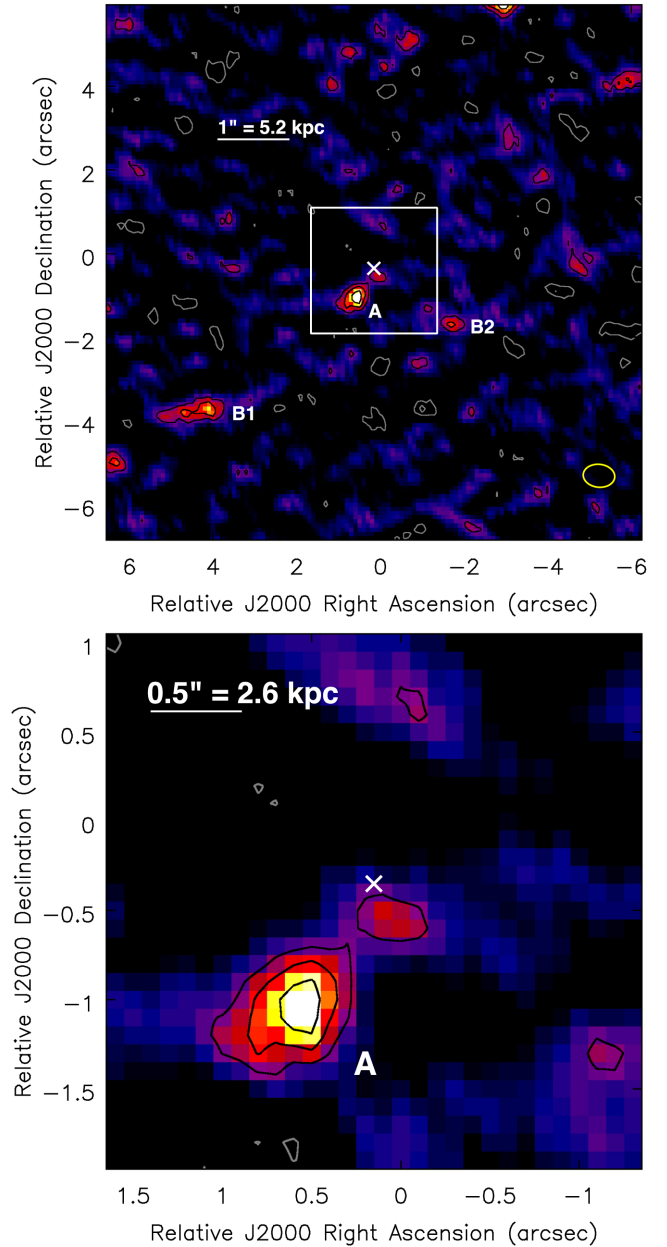
[1] This velocity is the average between the velocity estimated from a Gaussian fitting ($-64 \, \text{km s}^{-1}$) and the first moment of the line ($-78 \, \text{km s}^{-1}$).

Figure 3. Top: map of the [C II] emission obtained with a velocity interval of $100 \, \text{km s}^{-1}$, centred at $-64 \, \text{km s}^{-1}$ (relative to [C II] frequency expected from the Ly α redshift, $z = 7.109$), in the ALMA data of BDF3299. Black contours are at levels of 2, 3 and 4 times the noise per beam in the same map, i.e. 6.4 mJy beam^{-1} km s^{-1}. Grey contours are at the same levels, but for negative fluxes (note that -4σ is not reached anywhere). The ALMA beam is indicated in the bottom-right corner. The white cross indicates the location of the Y-band image centroid of the galaxy BDF3299. Label 'A' indicates the contours associated with the [C II] detection, whose spectrum is shown in Fig. 4, while 'B1' and 'B2' indicate two marginal detections discussed in the text. Bottom: zoom of the central 3 arcsec around the location of BDF3299. Note that the coordinates are relative to the phase centre of the ALMA observation in 2013, which was centred on the nominal coordinates of the optical image (but see the text for a discussion on the astrometry of the original Y-band images and their shift relative to the ALMA astrometry, which has been corrected here).
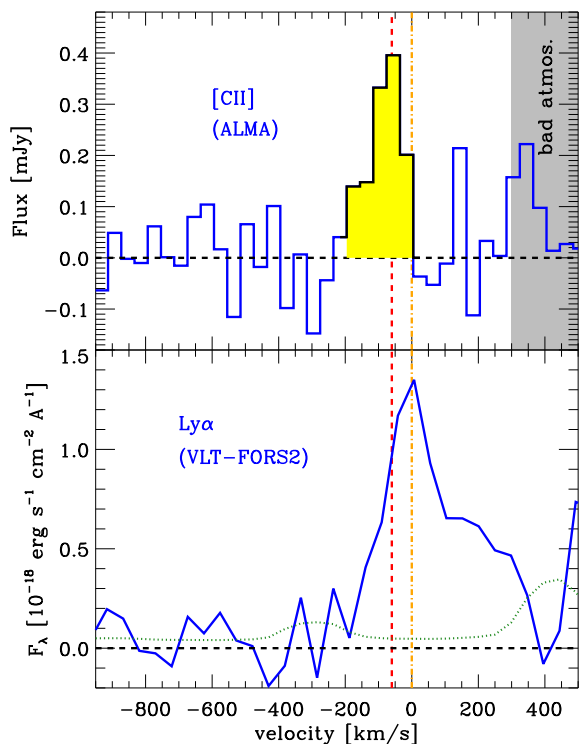
Figure 4. Top: ALMA spectrum of the [C II] source (clump 'A'), extracted from an elliptical aperture obtained by fitting the emission in the [C II] map (the spectrum flux has been corrected for the flux lost outside the extraction aperture, see text). The grey shaded region indicates the part of the spectrum affected by higher noise because of atmospheric absorption. Bottom: Ly α profile from the optical spectrum obtained by Vanzella et al. (2011). It should be noted the strongly asymmetric profile due to IGM absorption of the blue side of the line. The green dotted line indicates the sky background spectrum. Velocities are relative to the peak of Ly α (orange dot–dashed vertical line). The red dashed line indicates the velocity of the peak of the [C II] line.

4.2 Reliability of the detection

In this section, we discuss more in detail the significance of the [C II] detection.

First we have verified that the detection is not the result of a glitch in a single subset of the data. We have separated the visibilities obtained for BDF3299 in three data sets: the set of observations obtained in 2013 November, and we have divided into two halves the visibilities obtained in 2014 April. These three data subsets have similar depths (though the data in 2013 are somewhat shallower than each of the two halves data taken in 2014). We have verified that in each of these three data sets a signal of the [C II] line is seen, at a flux level consistent with the value observed in the merged data, within the noise of each individual subset of data. More specifically, by only taking the (more sensitive) data taken in 2014, the measured line flux is 46.0 ± 7.7 mJy km s^{-1}. If the 2014 data (four scans in total) are split in two groups of two scans each, then the line flux in each of the two scans is 44.7 ± 14.0 and 47.3 ± 12.7 mJy km s^{-1}. If only the (lower sensitivity) data taken in 2013 are used, then the measured line flux is 49.9 ± 17.9 mJy km s^{-1} (note that all of these fluxes, and associated errors, have been scaled by the same aperture correction factor of 2.5 discussed above).

We have then checked whether negative sources are detected with the same significance or not. We have searched for additional emission line detections within SPW1, within the spectral region between -1000 and $+300$ km s^{-1} (i.e. the region in which the noise is low and not affected by atmospheric absorption features). We have adopted the same velocity width (100 km s^{-1}) as for the [C II] detection, to extract maps for the initial selection of putative sources. We have restricted the search to this criterion both because the sidelobes of the continuum serendipitae may affect different velocity ranges in a different way, and because we have verified that the noise does not scale exactly as $(\Delta V)^{-1/2}$, possibly because of some residual baseline problems (see also Vio et al., in preparation, for a thorough analysis of the noise in the ALMA data). We have discarded putative detections (either positive or negative) for which: (1) the signal is not seen at the expected level (within the noise) in the three subsets of data discussed above (i.e. the detection is mostly resulting from a glitch in one or two of the three subsets of data); (2) the measured size of the putative detection is smaller than the synthesized beam, or (3) larger than 1.5 times the beam (real sources are not expected to be very extended). The latter two requirements come from the fact that a source with size significantly smaller (or much larger) than the synthesized beam must be due to noise associated with individual antennas, or group of antennas (these sources of noise are not correlated and therefore should give features with angular profiles much different than the beam). Sidelobes of serendipitae, or from strong sources outside the field of view, would also introduce features with sizes different from the beam. However, to be on the safe side, we have also excluded the region within 2 arcsec from the 0.4 mJy continuum serendipitous source, since the uncleaned continuum map shows some low-level sidelobe residuals in this area.

of 7σ. A summary of the [C II] line properties of clump A is given in Table 2.

We note that the same map in Fig. 3 reveals two potential additional marginal detections (B1 and B2), which are the only ones in the map with significance higher than 3σ within a radius of 6 arcsec and will be discussed later on.

The spatial location of the [C II] detection relative to the *Y*-band source is shown in Fig. 5, in which the green contours are the same as the (black) contours in Fig. 3, while the coloured background image is the *Y*-band image.

We note that at the location of the optical source the ALMA [C II] map shows a some signal at the 2σ level. However, this signal is very marginal and it will not be discussed any further.

Table 2. Parameters of the [C II] detection next to BDF3299 in clump 'A'.

$\nu_{obs}([C\,II])^a$ (GHz)	$z_{[C\,II]}$	ΔV^b (km s^{-1})	FWHM^b (km s^{-1})	$F([C\,II])$ (mJy km s^{-1})	$L([C\,II])$ (10^7 L$_\odot$)
234.43	7.107	-71 ± 10	102 ± 21	48.6 ± 6.9	5.9 ± 0.8

Notes. ^{a}Observed central frequency in LSRK. ^{b}Velocity offset relative to the peak of Ly α (ΔV) and FWHM are calculated both through the moment analysis and through a Gaussian fit; the values reported in the table are average values.
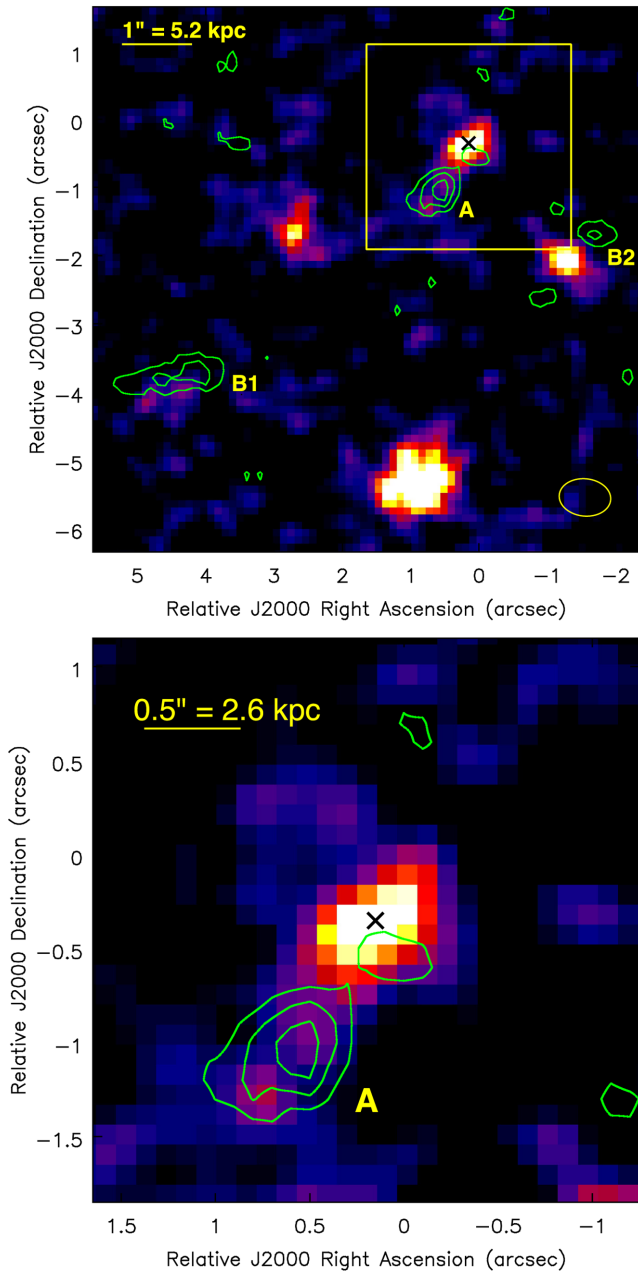
Figure 5. Top panel: the colour background image is the *Y*-band image of the BDF3299 field. The black cross indicates the location of the galaxy BDF3299 at $z = 7.109$. We recall that at this redshift the *Y*-band samples both Ly α and UV continuum. The green contours show the [C II] map with the same levels as (black contours) in Fig. 3. Label 'A' indicates the contours associated with the [C II] detection, whose spectrum is shown in Fig. 4, while 'B1' and 'B2' indicate two marginal detections discussed in the text. The ALMA beam is shown in the bottom-right corner. Bottom panel: zoom of the central 3 arcsec around the location of BDF3299. Note that the coordinates are relative to the phase centre of the ALMA observation in 2013, which was centred on the nominal coordinates of the optical image (but see the text for a discussion on the astrometry of the original *Y*-band images and their shift relative to the ALMA astrometry, which has been corrected here).

For each putative detection passing this screening we have extracted the spectra as for the [C II] detection and estimated the significance as discussed in Section 4.1 (i.e. over the same velocity interval of $200 \, \mathrm{km \, s^{-1}}$ as for our detection). The resulting distribution of the positive (red) and negative (blue) detections is shown, as a function of the signal-to-noise ratio (S/N), in the top panel of Fig. 6. The cumulative distribution of the positive and negative detections (i.e. the number of detection with significance above a given threshold) is shown in the middle panel of Fig. 6.

It is interesting to note that the number of positive detections at $>3\sigma$ is 30 per cent higher than the number of negative detections, suggesting that a significant fraction of the positive detections are real even down to the 3σ level. Focusing on the detections at $>5\sigma$, we note that there are no negative detections, hence giving further confidence that our positive detection at 7σ next to the optical position of the galaxy (clump 'A'), is real.

If we restrict the search within a radius of 3 arcsec from the optical location of BDF3299 (but still over the full velocity range $-1000 < \Delta V < +300 \, \mathrm{km \, s^{-1}}$), then the resulting distribution of detections is shown in the bottom panel of Fig. 6, in which there are only three potential positive detections, and no negative detections, above 3σ. This further supports the reliability of our detection in clump 'A'.

4.3 Line identification

The match of the line frequency with the one expected for [C II] at the redshift of BDF3299 (Fig. 4) strongly supports this identification of the line.

The identification with another transition associated with a foreground galaxy at lower redshift, which by chance happens to be at 0.7 arcsec from BDF3299, is extremely unlikely, since the sky density of molecular and atomic lines in this band, and with fluxes comparable with the line detected in our data, is extremely low. Even in such unlikely case, the galaxy should be clearly seen in the optical/near-IR images and in the thermal millimetre continuum. In the following we quantify these statements, hence excluding the line identification with a lower redshift transition.

The CO rotational transitions are the brightest transitions that can be seen in low/intermediate redshift galaxies at this frequency. Other transitions are generally much fainter. da Cunha et al. (2013a) have inferred the cumulative space density of CO transitions as a function of flux detection threshold.

We have considered their expectations including all CO rotational transitions from (7–6) to (2–1). da Cunha et al. (2013a) consider both the CO Spectral Line Energy Distribution (SLED) of the MW and the extreme CO SLED observed in the centre of the starburst galaxy M82. We have first conservatively adopted the CO SLED of the M82 centre; this is a conservative assumption, since the bulk of high-z galaxies have CO excitation closer to the MW (e.g. Dannerbauer et al. 2009). With this assumption we obtain that the cumulative probability of finding a CO emitter within a radius of 1 arcsec of a given position, within a velocity range of $\pm300 \, \mathrm{km \, s^{-1}}$ from a given frequency in band 6, and with a flux brighter than 30 mJy $\mathrm{km \, s^{-1}}$ (i.e. 50 per cent lower than the flux of the line detected by us), is about 10^{-4}.

If the CO SLED typical of the MW (which is closer to the CO SLED of the bulk of high-z galaxies) is taken, then the probability of chance CO detection drops to 2×10^{-5}, within a velocity interval of $\pm300 \, \mathrm{km \, s^{-1}}$, and to 7×10^{-6}, within a more reasonable velocity interval of $\pm100 \, \mathrm{km \, s^{-1}}$.
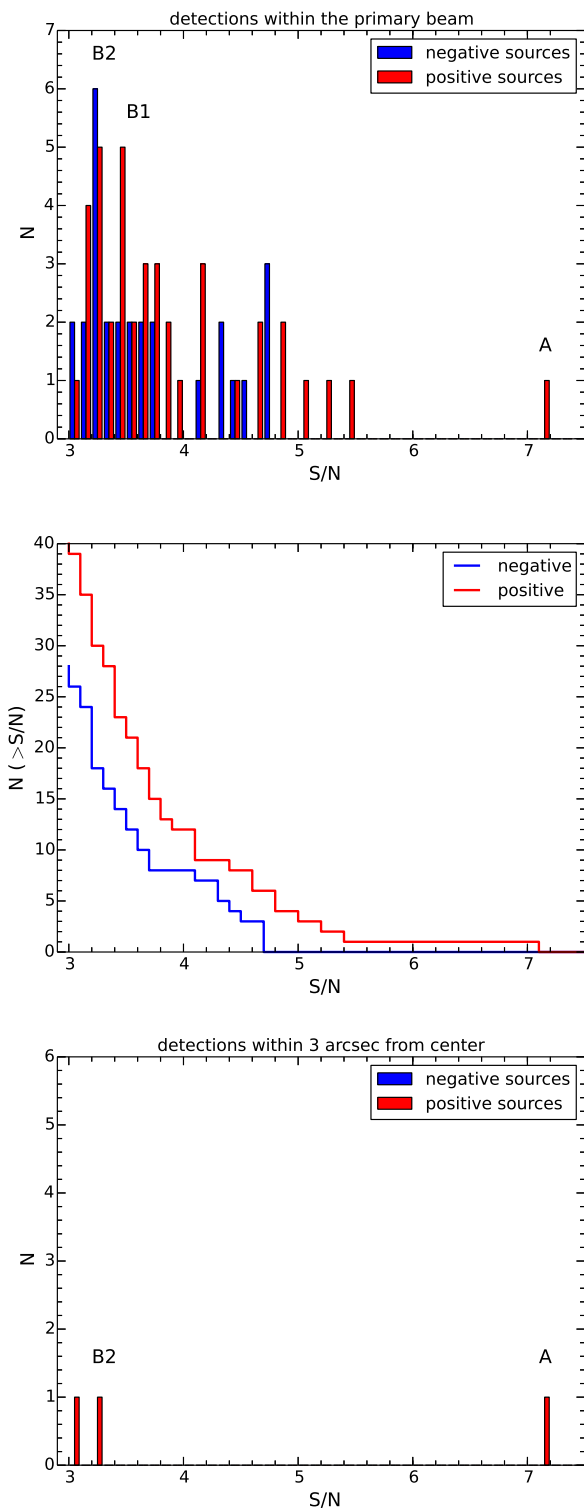
Figure 6. Top: distribution of positive (red) and negative (blue) detections in the SPW1 of BDF3299, as a function of S/N of the detection, for lines integrated over the same velocity range as our [C II] detection, searched within one primary beam and in the velocity range $-1000 < v < +300$ km s^{-1} (i.e. within the range of good atmospheric transmission). Middle: cumulative distribution of positive (red) and negative (blue) detections, within the same ranges. Bottom: distribution of positive (red) and negative (blue) detections within a radius of 3 arcsec from the position of BDF3299, and over the same velocity range $-1000 < v < +300$ km s^{-1}.

In the calculations above we have conservatively assumed the putative foreground galaxies to have solar metallicity, which has been used to estimate the CO sky densities. However, high redshift galaxies are characterized by lower metallicity than local galaxies (e.g. Maiolino et al. 2008). The CO-to-H$_2$ conversion factor depends steeply on metallicity (Bolatto, Wolfire & Leroy 2013), with low metallicity galaxies being much less efficient in emitting CO for a given molecular gas mass. Therefore, the probability of finding a foreground CO emitter in the vicinity of BDF3299, and at the same frequency expected for its [C II] emission, is even lower than inferred above.

In addition, to such extremely low probabilities of having a chance detection of a foreground, low-z CO emitter, one should take into account that a putative CO emission, with the intensity observed by us, should be associated with a relatively bright galaxy. Indeed, according to the Schmidt–Kennicutt law, CO emission tracing molecular gas in a galaxy, must be associated with a certain SFR. Assuming, for instance, that the observed line is CO(4–3) at $z = 1$ and conservatively assuming the S–K relation observed for local galaxies (Kennicutt & Evans 2012), one expects that the host galaxy should have a SFR ≈ 25 M$_\odot$ yr^{-1}. Such a SFR should be associated with a galaxy with a brightness in the Y band of $Y_{AB} = 20$ mag. However, there is not such bright counterpart at the location of the line detection. Beside BDF3299 itself, there is a faint source, marginally detected (Fig. 5), but confirmed in new *HST* images (Castellano et al., in preparation), located 0.3 arcsec to the south-east, but which is *seven magnitudes fainter* than expected. The faintness in the Y band could in principle be associated with extreme dust extinction. However, a SFR of 25M$_\odot$ yr^{-1} should also result into a 10σ continuum detection in our ALMA data, while we do not even have a marginal detection at the location of the line. Similar or even more extreme expectations are obtained for other CO transitions or for any other submm molecular or atomic transition.

These expected brightness in the Y band and in the millimetre should be considered as very conservative. Indeed, it has been shown that the S–K law evolves at high redshift, in the sense that for a given CO luminosity, or for a given gas content, high-z galaxies are characterized by higher SFR than local galaxies (Tacconi et al. 2013; Santini et al. 2014). High-z, low metallicity (faint) galaxies would be even more offset from the S–K relation, in the sense that their CO emission would be even fainter (because of the steep metallicity dependence of the CO-to-H$_2$ conversion factor) or, equivalently, for a given CO luminosity the associated SFR rate (hence Y band or far-IR continuum luminosity) should be even higher than estimated above.

Finally, the arguments above, based on the S–K law, apply to 'normal' galaxies. Starburst galaxies have an efficiency of star formation (SFR per unit gas mass) one order of magnitude higher (Daddi et al. 2010; Genzel et al. 2010). Therefore, depending on whether the putative foreground galaxy is 'normal' or 'starburst' the expected luminosity in any band should be a factor of a few, up to an order of magnitude, higher than estimated above.

Summarizing, the identification of the detected line with another transition associated with a foreground galaxy is extremely remote, leaving [C II] at $z = 7.107$ as the only realistic viable interpretation.

4.4 Interpretation of the [C II] emission

[C II] emission offset relative to the UV and Ly α emission was already been seen in some other high redshift galaxies (e.g. Gallerani et al. 2012; Williams et al. 2014), therefore our finding of offset [C II]

emission is not a novelty. However, previous cases were associated with peculiar objects, such as quasar host galaxies, or galaxies in an overdense environment and in the vicinity of a quasar. More recently such displacement between [C II] emisson and UV/Ly α emission has been observed also in high-z galaxies with more modest SFR (a few/several times 10 $M_\odot$ yr^{-1}), although still higher than the galaxies observed by us, and at lower redshifts, $5 < z < 6.1$ (Capak et al. 2015; Willott et al. 2015b).

Interestingly, displaced [C II] emission in primeval galaxies, as observed in our ALMA data, is an expected consequence of the strong stellar feedback that, according to many models, should characterize galaxy formation in the early Universe (e.g. Salvadori & Ferrara 2009; Dayal et al. 2014; Graziani et al. 2015). The [C II] line can be collisionally excited in many different ISM components (e.g. cold neutral medium, and high density PDRs in molecular clouds). However, negative (thermal, radiative, mechanical) feedback from stars can efficiently disperse or disrupt nearby molecular clouds, therefore quenching their [C II] PDR emission. In this case, [C II] emission can only arise from accreting/satellite clumps of neutral gas displaced from the primary galaxy main body.

To illustrate this scenario more quantitatively, in Fig. 7 a we show the model of primeval galaxies developed by Vallini et al. (2013), but specifically tailored to a galaxy at $z = 7.1$, with the same SFR as BDF3299. In this model the gas in the main galaxy is completely ionized, while molecular clouds (and the associated PDRs) are absent as a consequence of the strong stellar feedback (details on the model are summarized in Appendix B). The black points show the distribution of young hot stars, i.e. what we observe as UV rest-frame continuum emission (we recall that the rest-frame UV-emission contributes to 2/3 of the observed Y-band emission). The colour image shows the distribution of warm ionized gas, which can be observed as Ly α emission (note that the total observed Ly α emission can in principle be more extended as a consequence of scattering). The contours show the [C II]158 μm emission associated with the neutral gas (or mildly ionized gas). Clearly the central galaxy is expected to emit strong UV continuum and Ly α, but being completely photoionized, it does not emit any [C II]. However, very interestingly, the model expects [C II] emission from gas clumps at a few/several kpc ($\sim$ 1–2 arcsec) from the primary galaxy. These are satellite gas clumps in the process of accreting on to the primary galaxy, which have survived photoionization, owing to their distance from the source of UV photons (and because a significant fraction of UV photons are absorbed internally by the ISM of the primary galaxy).

Such [C II] emission in the satellite, accreting gas clumps is expected to be faint, but our deepest observation, the one of BDF3299, does have the sensitivity to detect it.

In Fig. 7b, we have smoothed the simulation to the angular resolution of our optical observations (0.5 arcsec seeing) and to the ALMA beam of our observations. The simulation is not meant, by any means, to exactly reproduce our observations (this would require a huge number of simulated objects with the same detailed modelling of the photoionization and radiative transfer (RT) in the ISM and IGM shown here, and then finding the best matching case). However, Fig. 7b illustrates that the offset between Y-band emission and [C II] emission is indeed expected to be resolved for various [C II] clumps (and especially for the brightest one) with the angular resolution delivered by our ALMA observation. Lower angular resolution observations would probably hamper the capability of resolving the spatial offset and would probably associate the [C II] emission with the primary UV–Ly α emitting galaxy.
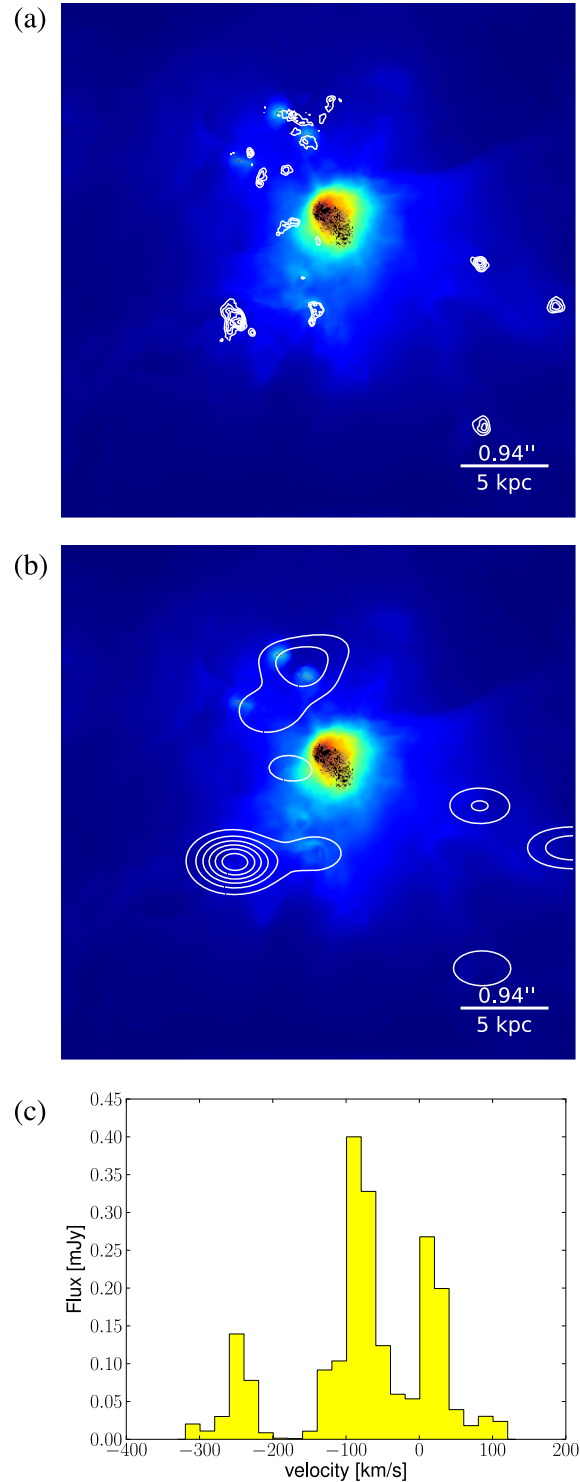

Figure 7. (a) Simulation of a primeval galaxy at $z = 7.1$ with SFR similar to BDF3299. The distribution of column density of ionized gas (which emits Ly α) is shown in colours (note that the observed diffuse Ly α emission can be more extended than the warm gas as a consequence of scattering). The black points show the distribution of young stars (UV continuum, which dominates the Y-band emission in our images). The contours show the emission of [C II] tracing the neutral gas (distributed in clumps orbiting/accreting the primary galaxy). (b) Same as the top panel in which the image of the ionized gas has been convolved with the angular resolution of our Y-band images (0.5 arcsec) and the [C II] map has been convolved with the ALMA beam of our data. (c) Integrated [C II] spectrum from the whole simulation.

The simulation also highlights that more than one [C II] clump may be present around BDF3299, out to 3 arcsec and possibly even at larger distances (3 arcsec is the maximum distance probed by the simulation box, so potential clumps at larger distances escape the simulation). If present, these clumps are probably below our detection limit and may also suffer beam dilution (many of the isolated small clumps disappear in the smoothed simulated map). Actually, in the ALMA cube of BDF3299 we find other positive [C II] detections, at lower significance than clump 'A', but in excess relative to the 'negative' detections, hence suggesting that they are not spurious detections. Two of such marginal detections are marked as B1 and B2 in Fig. 3. These are the two features with a peak flux detected at a significance higher than 3σ within a radius of 6 arcsec (half a beam radius) from the primary galaxy, in the same map, centred at -64 km s^{-1}. Certainly, deeper and/or higher angular resolution observations are required to further confirm these marginal detections.

In principle the line width and spatial extension can provide information on the dynamical mass of the blob. Determining a dynamical mass of the [C II] clump detected in the vicinity of BDF3299 is not easy, both because we do not know whether the line width is tracing a rotating system or a velocity dispersion dominated system, and because the [C II] map is only marginally resolved, hence the intrinsic dimension (beam deconvolved) is difficult to estimate. If we assume that the system is rotationally supported and with a radius of about 1.5 kpc (inferred from the Gaussian fit deconvolved from the beam in quadrature), we obtain a rough estimate of the clump dynamical mass of about 5×10^8 M$_\odot$. If the system is not virialized, then this is actually an upper limit to the dynamical mass. Although all the dynamical mass estimate is extremely uncertain, it suggests that indeed the [C II] clump is a small satellite of the primary galaxy.

According to the model, in these satellite/accreting clumps the [C II] excitation is not expected to primarily originate from *in situ* star formation, but mostly as a consequence of heating from the soft-UV irradiation from the central primary galaxy. This is consistent with the fact that we do not detect a clear *Y*-band source (i.e. Ly α+UV continuum) at the location of the [C II] clump. The vicinity of BDF3299 ($Y_{AB} = 26.15$) at 0.7 arcsec, and of another faint foreground galaxy at 0.4 arcsec ($Y_{AB} \approx 27.5$, see next section), prevent us to set tight upper limits on the *Y*-band emission associated with the [C II] clump, but it is certainly at least 3–4 times fainter than the primary galaxy. According to the [C II]–SFR relation for local (and intermediate redshift) galaxies (De Looze et al. 2014), the [C II] luminosity of the clump would imply a SFR ~ 6 M$_\odot$ yr^{-1}, i.e. comparable to the main galaxy BDF3299, i.e. the [C II] clump should have similar or higher *Y*-band flux. The inconsistency between the [C II] clump and the local [C II]–SFR relation is also illustrated in Fig. 2, which also shows the location of the [C II] clump, undetected in *Y* band, on the [C II]–SFR diagram. The clump is clearly inconsistent with the distribution of local galaxies, but it could still be marginally consistent with the expectations for low metallicity galaxies. Therefore, we cannot exclude some contribution to the [C II] excitation from *in situ* star formation, but we can also state that the non-detection of a clear *Y*-band counterpart is certainly consistent with the models expectations.

An alternative interpretation could be that the rest-frame UV emission associated with putative star formation in the [C II] clump is significantly obscured by dust. However, in this case one would expect associated dust emission at the level of ~ 15 μJy, which is ~ 2 times higher than the rms of the continuum map, while we currently do not even have a marginal continuum detection. We also note that the [C II] clump is not detected at longer wavelengths ($J_{AB} > 26.5$, $K_{AB} > 26.0$). Significant dust content responsible for significant extinction has also been generally excluded by various works on such high redshift galaxies (Walter et al. 2012; Ota et al. 2014; Capak et al. 2015; Schaerer et al. 2015b), as also discussed in this paper (in Section 5). However, the current data are not deep enough to completely exclude the scenario of dust obscuration. Additional data are certainly required to further dismiss or validate this possibility. Deeper *HST* data are currently being obtained and future *James Webb Space Telescope* data will certainly provide a definitive answer.

Obviously the clumps need some minimum level of metal enrichment to emit [C II]. The model suggests a metallicity of about 0.05 Z$_\odot$. However, the metallicity is very difficult to constrain by using a single emission line and especially based on [C II], since this one of the primary coolants of the ISM. Therefore, the metallicity of the neutral gas clumps is highly uncertain and additional data are required to properly constrain it. Here, we only note that a small level of metal enrichment in this clump may result either from pre-enrichment as a consequence of metals expelled from the primary galaxy, or from *in situ* production. Indeed, even a very low SFR of only 0.2 M$_\odot$ yr^{-1}, certainly undetectable by our observations (as discussed above), would be enough to enrich this small clump to a metallicity of ~ 0.05 Z$_\odot$ in less than 100 Myr.

Fig. 7c shows the integrated [C II] spectrum from the simulation. We note that the integrated [C II] spectrum inferred from the simulation, shown in Fig. 7c, expects additional narrow emission [C II] lines emitted from small accreting/satellite clumps illuminated by the primary source. We have tentatively identified narrower (10–20 km s^{-1}) [C II] emission sources in the vicinity of BDF3299, but which need to be confirmed with deeper and higher angular resolution observations.

The ALMA data of the other two sources in our sample (BDF521 and SDF46975) do not reveal clear evidence of [C II] emission in the vicinity of the UV–Lyα primary galaxy. However, the latter data are significantly shallower than the observation of BDF3299 (at least a factor of 2 in sensitivity). The same line seen in BDF3299 would be undetectable in the lower S/N observations of BDF521 and SDF46975.

Moreover, these two sources are brighter in the UV relative to BDF3299, hence their photoionization effect may extend to larger distances, therefore preventing neutral clouds to survive in the proximity of the galaxy.

4.5 Possible lensing from foreground galaxies

We already mentioned that a faint galaxy, marginally detected in the *Y* band (but confirmed by recent *HST* data, Castellano et al., in preparation), is found at 0.3 arcsec to the SE of the [C II] emitting clump. The galaxy is marginally detected also in the *V* band, so it must be a foreground galaxy, certainly not associated with the $z = 7.1$ system. Proper constraints on the redshift of this foreground galaxy will come from additional *HST* observations, as well as from forthcoming observations at the European Southern Observatory. Here, we note that finding a foreground galaxy so close to the ALMA line detection is intriguing.

The possibility that the line is actually CO at low redshift, and associated with this foreground galaxy, was already discussed and discarded above: both the extremely low sky density of CO emitters and the extremely faint counterpart (both in the *Y* band and in the millimetre continuum) make this scenario implausible. Here we only add, to the arguments discussed above, that the putative CO emission would be offset from the *Y*-band counterpart, which

would imply molecular gas offset by several kpc from the galaxy centre, which would be at odds with any known galaxy, where the molecular gas is found within the central few kpc of galaxies.

It is possible that the proximity of this source is simply resulting from a chance superposition. The source has a magnitude $AB \sim 27$ and density of sources at such faint fluxes is about 100 arcmin^{-2} mag^{-1} (Guo et al. 2013). The probability of randomly finding a galaxy with this magnitude, or brighter, within a radius of 0.3 arcsec of a given position is less than 10^{-2}. This probability is larger than that estimated for the chance CO detection discussed above, but still relatively small.

Another possible scenario is that the foreground low-z galaxy is gravitationally magnifying the [C II] emission at $z = 7.1$. Indeed, according to models, the primary galaxy at $z = 7.1$ should be surrounded by several [C II] emitting clumps. Although these clumps are abundant within a radius of $\sim$6 arcsec of the primary galaxy (30 kpc), the [C II] emission is probably below the detection threshold of our observations for most of them, especially as a consequence of their low metallicity. If a foreground galaxy happens to be in the field, this can introduce an even mild gravitational lensing that can boost the [C II] flux above our detection threshold.

This scenario would naturally explain the proximity of [C II] emission at $z = 7.1$ with a foreground galaxy, without invoking very unlikely chance overpositions. Indeed, in this scenario the several [C II] clumps become visible (their emission is boosted above the detection threshold) only when a foreground galaxy is located next to them in projection, so that some gravitational lensing can occur.

The effect is particularly effective if the foreground galaxy is at $z = 1.5$, which is the redshift maximizing the lensing magnification of radiation at $z = 7.1$. Unfortunately we do not have elements to test this scenario more quantitatively, since we do not yet have information on the redshift, mass and light profile of the putative lensing galaxy and we do not have high enough resolution ALMA observations to properly investigate the morphology of the putative lensed emission. Therefore, for the time being this has to be regarded as a speculation, which would explain the observations, but to be tested with additional data.

However, in support of this lensing scenario, we note that the other two marginal [C II] detections in the vicinity of BDF3299 (B1 and B2 in Fig. 3), are also found within 0.4 arcsec of two foreground galaxies, as seen in Fig. 5. The galaxy next to B1 is only marginally detected in our *Y*-band image, but it is confirmed in new *HST* data (Castellano et al., in preparation). The galaxy next to B2 is clearly detected and the data currently available give an approximate photometric redshift $z_{phot} \sim 1$, which is consistent with the lensing scenario.

The cumulative probability of having, by random chance superposition, three *Y*-band detections within 0.4 arcsec of three given positions (our [C II] detection 'A' and the other two marginal [C II] detections 'B1' and 'B2') is 10^{-6}. The lensing scenario would instead naturally explain the co-location of [C II] emission and foreground galaxies, without having to invoke extremely low chance probabilities.

Certainly additional data are required to confirm and quantitatively test the lensing scenario.

5 CONTINUUM DUST EMISSION

While we have found a few serendipitous continuum detections (Carniani et al. 2015), the continuum dust thermal emission is not detected in any of our galaxies. This result is in line with previous
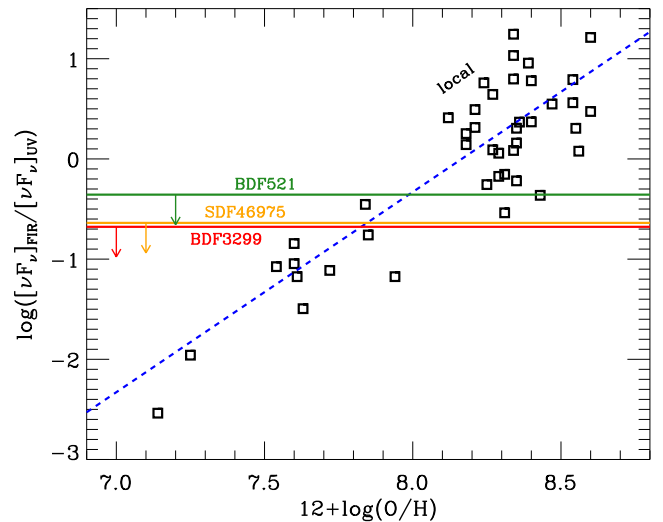

Figure 8. Far-IR ($\lambda_{rest} = 160\,\mu m$) to far-UV ($\lambda_{rest} = 1500$Å) luminosity ratio for local galaxies as a function of metallicity (black symbols). The blue dashed line is a linear fit to the data. The coloured solid lines indicate the upper limits on $(\nu F_\nu)_{FIR}/(\nu F_\nu)_{UV}$ inferred for the sample of our galaxies at $z \sim 7$, specifically: red for BDF3299, orange for SDF46975, green for BDF521.

results at high redshift (Walter et al. 2012; Ota et al. 2014; Schaerer et al. 2015b), which have found that distant 'normal' star-forming galaxies, close to the re-ionization epoch, have a rest-frame far-IR/UV luminosity ratio significantly lower relative to the bulk of local star-forming galaxies, with upper limits on the far-IR emission typically consistent with local low-metallicity dwarf or irregular galaxies. This suggests that these early systems are characterized by a small content of dust (which should reprocess UV light into IR thermal emission), both because of their low metallicity and because of shortage of time to produce dust (Nozawa et al. 2007; Valiante et al. 2009, 2011; Hirashita et al. 2014; Schneider et al. 2014). Our non-detections go in the same direction, but achieving even tighter upper limits on the far-IR/UV luminosity ratio.

Fig. 8 shows the ratio $(\nu F_\nu)_{FIR}/(\nu F_\nu)_{UV}$ versus galaxy metallicity for local galaxies, where $(\nu F_\nu)_{UV}$ is estimated at $\lambda_{rest} = 1530$Å (i.e. *GALEX* far-ultraviolet (FUV) band, for galaxies in the local Universe), and $(\nu F_\nu)_{FIR}$ is estimated at $\lambda_{rest} = 160\,\mu m$ [i.e. the longest wavelength band of the *Herschel* Photodetector Array Camera and Spectrometer (PACS), for local galaxies]. Data are taken from Dale et al. (2007), Dale et al. (2012), Ota et al. (2014, and private communication) and from Moustakas et al. (2010, in the latter we have used the calibrations from Pilyugin & Thuan 2005). We have applied the correction to the far-IR fluxes, as discussed in Ota et al. (2014) and da Cunha et al. (2013b), to take into account the fact that at high redshift the detectability of thermal emission is more difficult because of the cosmic microwave background (CMB) temperature being non-negligible relative to the dust temperature in galaxies (for the sake of simplicity we have adopted the same correction assuming all three sources at $z = 7$). For local galaxies, there is a clear trend of $(\nu F_\nu)_{FIR}/(\nu F_\nu)_{UV}$ to increase with metallicity, implying that a larger fraction of the UV light is reprocessed by dust at high metallicities. This is very likely a consequence of the dust content scaling with metallicity (e.g. Draine et al. 2007; Rémy-Ruyer et al. 2014). The blue dashed line is a linear fit to the data in the log–log plane. The 3σ upper limits on the $(\nu F_\nu)_{FIR}/(\nu F_\nu)_{UV}$ on $z \sim 7$ sources are indicated with horizontal coloured lines (see legend). Clearly, galaxies

Table 3. Constraints on the continuum upper limits.

Name	$(\nu F_\nu)_{FIR}/(\nu F_\nu)_{UV}^a$	$M_{dust}(T = 27.6\,K)$ $(10^7 M_\odot)$	$M_{dust}(T = 45\,K)$ $(10^7 M_\odot)$
BDF-3299	<0.21	<2.1	<0.32
BDF-512	<0.44	<5.2	<0.77
SDF-46975	<0.23	<5.8	<0.87

Notes. $^a(\nu F_\nu)_{FIR}$ is estimated at $\lambda_{rest} = 160\,\mu m$, $(\nu F_\nu)_{UV}$ is estimated at $\lambda_{rest} = 1500\,Å$.

at $z \sim 7$ are inconsistent with the UV-to-IR Spectral Energy Distribution (SED) of typical local galaxies, with solar-like metallicities, but are consistent with metal-poor (hence dust-poor) local dwarf galaxies, with metallicities about seven times lower than solar. Yet, while this suggests that the $z \sim 7$ galaxies in our sample must have metallicities similar or lower than local metal-poor dwarfs, the latter typically have SFR's one or two orders of magnitude lower than the sources observed by us. Therefore, the galaxies observed by us at $z = 7.1$ are probably scaled up versions (by at least an order of magnitude) of local low metallicity dwarfs.

Constraints on the dust mass are in principle physically more interesting. However, it is not possible to obtain an upper limit on the dust mass based on a single upper limit on the rest-frame far-IR or submm emission, since the dust temperature is not known. Ota et al. (2014) assumes a dust temperature of 27.6 K (and an emissivity index $\beta = 1.5$) resulting from the average of 17 local dwarf and irregular galaxies. Schaerer et al. (2015b) assume a range of temperatures between 25 and 45 K. We follow a similar approach as these papers to infer an upper limit on the dust mass from our 3σ upper limits at $\lambda_{obs} = 1.2$ mm, corrected for the effects of CMB. Depending on the assumed dust temperatures we obtain upper limits on the dust mass in the range between a few times 10^6 $M_\odot$ and several times 10^7 $M_\odot$, as detailed in Table 3. We note that such low dust content is in agreement with the finding that the SFR inferred from Ly α is consistent, within uncertainties, with the SFR inferred from the UV emission (Vanzella et al. 2011).

In the early universe the dust content is not only determined by the metallicity, but also by time-scale issues associated with the dust production mechanisms. Indeed, AGB stars, which are thought to be the main factory of dust in the local universe (e.g. Ventura et al. 2012b,a; Di Criscienzo et al. 2013; Schneider et al. 2014), require a time-scale of several 100 Myr to evolve and to contribute significantly to the dust content, hence a time-scale comparable to the age of the universe at $z \sim 7$. Dust forming in the ejecta of core-collapse supernovae can be an additional source of dust on very short time-scales, and indications that SN dust can indeed contribute significantly to the overall dust budget in the early universe, has been found by observational studies (e.g. Maiolino et al. 2004; Stratta et al. 2007; Gallerani et al. 2010; Stratta, Gallerani & Maiolino 2011). Extensive models have been developed to investigate the expected dust evolution in primordial galaxies (e.g. Valiante et al. 2009, 2011; Gall, Andersen & Hjorth 2011; Hirashita et al. 2014; Nozawa et al. 2015). Our tight upper limits on the dust mass in these early systems further suggest that at these early epochs primeval galaxies have little time to produce masses of dust comparable with lower redshift galaxies. A more quantitative comparison with models of dust formation in the early universe goes beyond the scope of this paper and will be discussed in other forthcoming papers (Valiante et al., in preparation; Ferrara et al., in preparation).

6 CONCLUSIONS

We have presented new ALMA millimetre observations aimed at constraining the [C II]158 μm and thermal dust continuum emission in three primeval galaxies at $z \sim 7$, whose redshift had been spectroscopically confirmed through the detection of (asymmetric) Ly α. In contrast to many previous millimetre observations of high redshift galaxies, which have targeted galaxies with extreme SFR (100–1000 $M_\odot$ yr^{-1}), the galaxies in our sample have SFR $\sim$5–15$M_\odot$ yr^{-1}, more typical of the bulk of galaxies at these early epochs.

At the location of the optical (*Y*-band) counterpart, which samples the rest-frame Ly α and UV emission, no [C II]158 μm line emission is detected. For some of the galaxies the 3σ upper limit on the [C II] luminosity is significantly lower than what is observed in local galaxies with similar SFR, even including many metal-poor local galaxies The upper limit on the [C II]/SFR ratio in these galaxies is also lower than observed in galaxies at $z \sim 5$–6.

However, in the deepest of our ALMA observations, targeting the highest redshift galaxy of our sample (BDF3299 at $z = 7.109$) we do detect [C II] emission, slightly spatially offset, by 0.7 arcsec (4 kpc), relative to the optical (*Y*-band) counterpart.

The line is detected at 7σ. The level of confidence is verified by checking the detection in subsets of the same data, by checking the absence of any negative detection at confidence level higher than 5σ in data cube over the whole ALMA primary beam and over a broad frequency interval, as well as the absence of any negative detection at a confidence level higher than 3σ within a radius of 3 arcsec from the optical source.

The detection of [C II] spatially offset from the optical galaxy, along with the absence of [C II] emission at the location of the optical counterpart, is in nice agreement with the predictions of recent models of galaxy formation in the early universe. According to these models, strong negative stellar feedback in these primeval systems quickly destroys or disperses molecular clouds, hence quenching the emission of [C II] (the bulk of carbon is therefore in higher ionization states). However, [C II] emission arises from accreting/satellite clumps of neutral gas displaced from the primary galaxy main body.

Therefore, our ALMA observations are directly probing such early phases of galaxy formation, in which both stellar feedback and gas accretion are at work.

In the accreting clump [C II] emission is likely resulting primarily as a consequence of heating by the strong UV radiation from the primary galaxy. However, some contribution to the [C II] excitation from *in situ* star formation cannot be excluded.

At larger distances from the same galaxy ($\sim$ 2–4 arcsec, i.e. $\sim$10–20 kpc), we obtain two additional marginal [C II] detections at the redshift consistent with Ly α. These marginal detections need to be confirmed with additional data, but their presence would be in line with the expectations of the models discussed above, according to which several satellites clumps of neutral gas should be

emitting faint [C II] line in the surrounding of the primary primeval galaxy.

It is interesting that both the [C II] detection and the two marginal detections are located in the vicinity (within 0.3–0.5 arcsec) of foreground galaxies at lower redshifts. We show that the association of the millimetre lines with other transitions at lower redshift (in particular CO transitions) is extremely remote and inconsistent with the properties of the counterparts (in terms of SFR). Chance superposition coincidence is possible, but very unlikely. We suggest, as an alternative explanation, that gravitational lensing by foreground galaxies may boost the flux of the [C II] clumps located in the vicinity of the primary $z = 7.1$ galaxy, hence bringing them above the detection threshold. Testing this scenario more quantitatively requires a deeper knowledge of the properties of the foreground galaxies (redshifts, masses, mass profile distribution, etc.) and higher angular resolution data of the [C II] emission. However, if confirmed, this scenario would indicate that lensing from foreground galaxies at $z \sim 1$–2 could be an effective way to detect faint neutral clumps of accreting gas in the vicinity of primeval galaxies around re-ionization.

Continuum thermal emission is not detected in any of the three galaxies of our sample. The 3σ upper limit on the (rest-frame) IR-to-UV continuum emission ratio is consistent with the value observed for the lowest metallicity local galaxies, in which the dust content is very low. Constraints on dust masses are difficult to infer, because only one single photometric upper limit per source is available for the IR SED, hence no constraints on the dust temperature are available. By assuming the dust temperature typical of local low metallicity galaxies, we obtain 3σ upper limits on the dust masses of a few times $10^7 M_{dust}$. The latter confirms that these early systems have a very low dust content, both because of low metallicity and because of shortage of time to produce dust at these early epochs through some of the standard dust production channels.

REFERENCES

Appleton P. N. et al., 2013, ApJ, 777, 66
Baek S., Di Matteo P., Semelin B., Combes F., Revaz Y., 2009, A&A, 495, 389
Bolatto A. D., Wolfire M., Leroy A. K., 2013, ARA&A, 51, 207
Bothwell M. S. et al., 2013, ApJ, 779, 67
Bouwens R. J. et al., 2004, ApJ, 606, L25
Capak P. L. et al., 2015, preprint (arXiv:1503.07596)
Carilli C. L., Walter F., 2013, ARA&A, 51, 105
Carilli C. L., Riechers D., Walter F., Maiolino R., Wagg J., Lentati L., McMahon R., Wolfe A., 2013, ApJ, 763, 120
Carniani S. et al., 2013, A&A, 559, A29
Carniani S. et al., 2015, preprint (arXiv:1502.00640)
Castellano M. et al., 2010, A&A, 524, A28
Cicone C. et al., 2015, A&A, 574, A14
Cormier D. et al., 2012, A&A, 548, A20
da Cunha E. et al., 2013a, ApJ, 765, 9
da Cunha E. et al., 2013b, ApJ, 766, 13
Daddi E. et al., 2010, ApJ, 714, L118
Dale D. A. et al., 2007, ApJ, 655, 863
Dale D. A. et al., 2012, ApJ, 745, 95
Dannerbauer H., Daddi E., Riechers D. A., Walter F., Carilli C. L., Dickinson M., Elbaz D., Morrison G. E., 2009, ApJ, 698, L178
Dayal P., Ferrara A., Dunlop J. S., Pacucci F., 2014, MNRAS, 445, 2545
De Breuck C., Maiolino R., Caselli P., Coppin K., Hailey-Dunsheath S., Nagao T., 2011, A&A, 530, L8
De Breuck C. et al., 2014, A&A, 565, A59
De Looze I. et al., 2014, A&A, 568, A62
Di Criscienzo M. et al., 2013, MNRAS, 433, 313
Draine B. T. et al., 2007, ApJ, 663, 866
Finkelstein S. L. et al., 2012, ApJ, 758, 93
Gall C., Andersen A. C., Hjorth J., 2011, A&A, 528, A14
Gallerani S. et al., 2010, A&A, 523, A85
Gallerani S. et al., 2012, A&A, 543, A114
Gallerani S., Ferrara A., Neri R., Maiolino R., 2014, MNRAS, 445, 2848
Genzel R. et al., 2010, MNRAS, 407, 2091
González-López J. et al., 2014, ApJ, 784, 99
Graciá-Carpio J. et al., 2011, ApJ, 728, L7
Graziani L., Salvadori S., Schneider R., Kawata D., de Bennassuti M., Maselli A., 2015, MNRAS, 449, 3137
Guo Y. et al., 2013, ApJS, 207, 24
Hezaveh Y. D. et al., 2013, ApJ, 767, 132
Hirashita H., Ferrara A., Dayal P., Ouchi M., 2014, MNRAS, 443, 1704
Kaufman M. J., Wolfire M. G., Hollenbach D. J., Luhman M. L., 1999, ApJ, 527, 795
Kennicutt R. C., Evans N. J., 2012, ARA&A, 50, 531
Leitherer C. et al., 1999, ApJS, 123, 3
Madden S. C., Poglitsch A., Geis N., Stacey G. J., Townes C. H., 1997, ApJ, 483, 200
Madden S. C. et al., 2011, in Röllig M., Simon R., Ossenkopf V., Stutzki J., eds, EAS Publ. Ser. Vol. 52, The Elusive ISM of Dwarf Galaxies: Excess Submillimetre Emission & CO-Dark Molecular Gas. EDP Sciences, Les Ulis, p. 95
Maiolino R., Schneider R., Oliva E., Bianchi S., Ferrara A., Mannucci F., Pedani M., Roca Sogorb M., 2004, Nature, 431, 533
Maiolino R. et al., 2005, A&A, 440, L51
Maiolino R. et al., 2008, A&A, 488, 463
Maiolino R., Caselli P., Nagao T., Walmsley M., De Breuck C., Meneghetti M., 2009, A&A, 500, L1
Maiolino R. et al., 2012, MNRAS, 425, L66
Malhotra S. et al., 2001, ApJ, 561, 766
Moustakas J., Kennicutt R. C., Jr, Tremonti C. A., Dale D. A., Smith J.-D. T., Calzetti D., 2010, ApJS, 190, 233
Nagao T., Maiolino R., Marconi A., Matsuhara H., 2011, A&A, 526, A149+
Negrello M. et al., 2010, Science, 330, 800
Nozawa T., Kozasa T., Habe A., Dwek E., Umeda H., Tominaga N., Maeda K., Nomoto K., 2007, ApJ, 666, 955
Nozawa T., Asano R. S., Hirashita H., Takeuchi T. T., 2015, MNRAS, 447, L16
Oesch P. A. et al., 2015, ApJ, 804, L30
Ono Y. et al., 2012, ApJ, 744, 83
Ota K. et al., 2014, ApJ, 792, 34
Ouchi M. et al., 2009, ApJ, 706, 1136
Ouchi M. et al., 2013, ApJ, 778, 102

Pettini M., Rix S. A., Steidel C. C., Adelberger K. L., Hunt M. P., Shapley A. E., 2002, ApJ, 569, 742

Pilyugin L. S., Thuan T. X., 2005, ApJ, 631, 231

Pineda J. L., Langer W. D., Goldsmith P. F., 2014, A&A, 570, A121

Rémy-Ruyer A. et al., 2014, A&A, 563, A31

Riechers D. A. et al., 2014, ApJ, 796, 84

Robertson B. E., Ellis R. S., Furlanetto S. R., Dunlop J. S., 2015, ApJ, 802, L19

Röllig M., Ossenkopf V., Jeyakumar S., Stutzki J., Sternberg A., 2006, A&A, 451, 917

Salvadori S., Ferrara A., 2009, MNRAS, 395, L6

Salvaterra R., Ferrara A., Dayal P., 2011, MNRAS, 414, 847

Santini P. et al., 2014, A&A, 562, A30

Sargsyan L. et al., 2012, ApJ, 755, 171

Schaerer D. et al., 2015a, A&A, 576, L2

Schaerer D., Boone F., Zamojski M., Staguhn J., Dessauges-Zavadsky M., Finkelstein S., Combes F., 2015b, A&A, 574, A19

Schneider R., Valiante R., Ventura P., dell'Agli F., Di Criscienzo M., Hirashita H., Kemper F., 2014, MNRAS, 442, 1440

Springel V., Di Matteo T., Hernquist L., 2005, MNRAS, 361, 776

Stratta G., Maiolino R., Fiore F., D'Elia V., 2007, ApJ, 661, L9

Stratta G., Gallerani S., Maiolino R., 2011, A&A, 532, A45

Swinbank A. M. et al., 2014, MNRAS, 438, 1267

Tacconi L. J. et al., 2013, ApJ, 768, 74

Valiante R., Schneider R., Bianchi S., Andersen A. C., 2009, MNRAS, 397, 1661

Valiante R., Schneider R., Salvadori S., Bianchi S., 2011, MNRAS, 1149

Vallini L., Gallerani S., Ferrara A., Baek S., 2013, MNRAS, 433, 1567

Vallini L. et al., 2015, submitted

Vanzella E. et al., 2011, ApJ, 730, L35

Velusamy T., Langer W. D., 2014, A&A, 572, A45

Venemans B. P. et al., 2012, ApJ, 751, L25

Ventura P. et al., 2012a, MNRAS, 424, 2345

Ventura P. et al., 2012b, MNRAS, 420, 1442

Wagg J. et al., 2012, ApJ, 752, L30

Walter F., Riechers D., Cox P., Neri R., Carilli C., Bertoldi F., Weiss A., Maiolino R., 2009, Nature, 457, 699

Walter F. et al., 2012, ApJ, 752, 93

Wang R. et al., 2013, ApJ, 773, 44

Williams R. J. et al., 2014, MNRAS, 439, 2096

Willott C. J., Omont A., Bergeron J., 2013, ApJ, 770, 13

Willott C. J., Carilli C. L., Wagg J., Wang R., 2015b, preprint (arXiv:1504.05875)

Willott C. J., Bergeron J., Omont A., 2015a, ApJ, 801, 123

Wolfire M. G., Hollenbach D., McKee C. F., Tielens A. G. G. M., Bakes E. L. O., 1995, ApJ, 443, 152

Wolfire M. G., McKee C. F., Hollenbach D., Tielens A. G. G. M., 2003, ApJ, 587, 278

APPENDIX A: CONTINUUM SERENDIPITAE AND REGISTRATION WITH THE OPTICAL IMAGES

The continuum map of BDF3299 reveals three serendipitous detections (Carniani et al. 2015): two detections within the primary beam (one at ∼40σ and another one at ∼6σ) and a third detection outside the primary beam (at ∼4σ). Fig. A1 shows the continuum maps of the two detections within the primary beam. Both detections have counterpart in the near-IR images (either *Y* band or *K* band). However, the centroid of the near-IR counterparts is slightly offset relative to the millimetre emission in the ALMA map. This is visible in Fig. A1 where the white crosses show the location of the near-IR counterparts (in images which are not yet registered as discussed in Section 2). Clearly both counterparts are offset by a similar amount and in the same direction and more specifically by about 0.4 arcsec towards the NW (PA∼343°). Since these offsets are
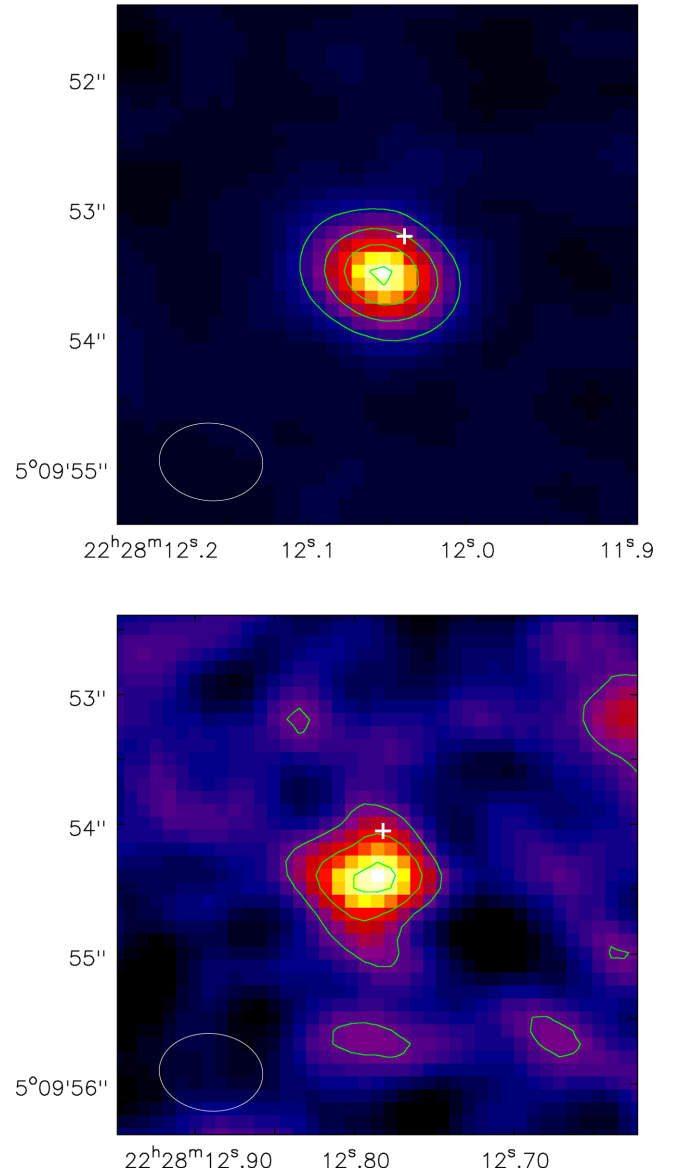

Figure A1. Top: continuum map of the brightest serendipitous source detected in the field of BDF3299. Contours are at of 10σ, 20σ, 30σ, 40σ, where the rms = 7.8 μJy. Bottom: continuum map of the second brightest serendipitous source in the same field. Contours are at of 2σ, 4σ, 6σ. In both panels the white cross indicates the location of the near-IR counterpart.

the same for both continuum sources we believe they are associated with an offset of the astrometry of the near-IR images relative to the ALMA images. We have therefore corrected for such an offset when comparing the ALMA and near-IR images.

APPENDIX B: THE THEORETICAL MODEL

A detailed description of the model and simulations used in this paper is given in Vallini et al. (2013). In this appendix we only summarize some of the key points.

The Vallini et al. (2013) model is based on cosmological smoothed particle hydrodynamic simulations performed with GADGET-2 (Springel, Di Matteo & Hernquist 2005). The original simulation reproduces a $(10 \, h^1 \, \text{Mpc})^3$ comoving volume with 2×512^3 baryonic+dark matter particles, giving a mass resolution

of 1.32×10^5 M$_\odot$ for baryons and 6.68×10^5 M$_\odot$ for dark matter. We select a snapshot at redshift $z \sim 7$, and we identify the most massive halo (total mass $M_h = 1.17 \times 10^{11}$ M$_\odot$, $r_{vir} \approx 20$ kpc) by using a Friend-of-Friend algorithm. We then zoom the simulation by selecting a $(0.65 \, h^1 \, \text{Mpc})^3$ comoving volume around the centre of the halo, and post-process UV RT using LICORICE (Baek et al. 2009). Gas properties are resolved on a fixed grid with a resolution of 60 pc. To define the position of the ionizing sources we assume that stars form in those cells characterized by a gas density $\rho > 1$ cm^{-3} in order to reproduce the typical size ($\sim$1–2 kpc) of star-forming regions at $z \approx 6$–7 (Bouwens et al. 2004; Ouchi et al. 2009), as inferred by UV continuum images. The population synthesis code STARBURST99 (Leitherer et al. 1999) is used to obtain the ionizing spectrum of the galaxy.

The simulation is complemented with a subgrid model taking into account the cooling and heating processes producing two-phase thermal structure of the neutral gas in the ISM (as in Wolfire et al. 1995, 2003). The density (n_{CNM}, n_{WNM}) and temperature (T_{CNM}, T_{WNM}) of the the cold (CNM) and warm (WNM) neutral phase in each cell of the simulation is calculated as a function of (1) the gas metallicity, Z, determining the coolants abundance, and (2) the FUV flux, G_0, in the Habing (6–13.6 eV) band, controlling the photoelectric heating produced by dust grains. G_0 scales with the SFR and depends on the assumed age of the stellar population. The density and temperature of the CNM and WNM allow us to compute [C II] emissivity from each cell of the simulated galaxy as in equation (2) in Vallini et al. (2013).

Variations of such model in which molecular gas and PDR are present in the main galaxy are presented in Vallini et al. 2015, submitted.

This paper has been typeset from a TeX/LaTeX file prepared by the author.